


Adaptable Flight Line Planning for Airborne Photogrammetry Using DEM

Haitao Zhao , Bing Zhang, *Fellow, IEEE*, Wenmin Hu, Jianguai Liu, Dong Li, Yalin Liu, Hong Yang, Jie Pan, and Liuqing Xu

Abstract—Flight line planning is the first step in an aerial photography campaign. Its two key parameters, ground sampling distance (GSD), and overlap should be designed carefully as they will impact subsequent flying workload and even the final mapping accuracy. For a flat terrain region, flight line planning is easy using a traditional method with fixed baseline, flight spacing, and flight altitude. But for a steep terrain region, photo overlap and GSD will change greatly with topography, and thus a flight line planning using the traditional method is not sufficient. This article presents a novel adaptable flight line planning method for frame camera with four application modes. The flight line planning procedure is implemented through rigorous imaging geometry model using digital elevation data, where actual overlap and GSD can be calculated precisely. Using the desired overlap and GSD as constraint conditions, the flight spacing, baseline, and flight altitude can be adjusted adaptively according to ground topography. To assess the effect, a hypothetical test in a rugged terrain region was conducted to compare the project workload, GSD, and overlap of the four modes. The results show that Mode 2, Mode 3, and Mode 4 can realize better overlap with lower workload than the traditional method Mode 1. Mode 3 and Mode 4 have better GSD distribution than Mode 1 and Mode 2. The Mode 3 method was also validated in an actual project, showing a favorable performance in final reality 3D model result.

Index Terms—Airborne photogrammetry, digital elevation model (DEM), flight line planning, overlap, terrain following, variable baseline.

I. INTRODUCTION

AIRBORNE remote sensing imagery is widely used for mapping, environmental monitoring, ecological protection, hazard responses, and so on [1]. Nowadays, multimodal

airborne imagery is also an important data source for deep learning approaches to extract high-quality information [2]–[4]. An appropriate planning of a flight mission is a fundamental prerequisite for a successful acquisition of airborne imagery [5], [6]. Flight line planning is the first step for the airborne photogrammetry. Determining an appropriate setting for flight is essential, as different combinations of flight parameters influence the flying workload, the quality, and usability of final products [7]–[10]. The planning quality and flying quality will impact the subsequent mapping task directly [11], [12]. Flight line planning has two important planning quality parameters: the ground sampling distance (GSD) and the overlap which consists of the endlap and sidelap for frame cameras. A favorable flight line planning is that GSD should be as constant as possible, and the overlap should be as close as possible to the desired value. For a flat terrain region, this is not difficult to achieve using a traditional approach, with a constant baseline and flight spacing. But, for a rugged terrain region, photo overlap will vary substantially if a constant baseline and flight spacing is adopted. For a traditional stereo-mapping task, if GSD changes a lot, the accuracy will decrease below the desired level at the coarser GSD subregion. If overlap is too small, gap may be resulted, which leads to serious failure of aerial photography, whereas if the overlap is too big, the intersection geometry is poor, which will change the base–height ratio and decrease the height accuracy from error propagation model for stereomapping on the one hand [13] and also induce data redundancy and increase workload on the other.

Traditionally, about 30 years ago in the film camera era, flight line planning is manually conducted using a map. First, terrain elevations of many typical points are measured and the reference terrain elevation is determined. If the terrain elevation changes hugely, the region should be divided into several subregions to plan flight lines respectively. It is a time-consuming manual work in which a well-trained expert is needed. Usually the flight lines are calculated manually to make sufficient sidelap, but the camera exposure points (also called waypoints) are not determined, because there is no equipment to trigger the camera at the planned point. Triggering of the camera is controlled manually by spiral mode to retain the constant endlap, which is a laborious work of a camera operator [14].

About 20 years ago, with the development of digital mapping and the GPS navigation technologies, flight line planning became much easier. Several professional aerial photography flight planning softwares have been developed, e.g., Leica ASCOT, IGI IGIplan, and TrackAir SnapPLAN [15]–[17]. The flight

Manuscript received March 25, 2021; revised May 14, 2021 and May 22, 2021; accepted June 6, 2021. Date of publication June 10, 2021; date of current version June 30, 2021. This work was supported by the Youth Innovation Promotion Association of CAS under Grant Y8YR2700QM and Airborne Observation System Application Calibration and Validation Project of CHEOS under Grant 30-H30C01-9004-19/21. (*Corresponding author: Bing Zhang.*)

Haitao Zhao, Bing Zhang, Dong Li, Hong Yang, Jie Pan, and Liuqing Xu are with the Aerospace Information Research Institute, Chinese Academy of Sciences, Beijing 100094, China (e-mail: zhaoh@aircas.ac.cn; zhangbing@aircas.ac.cn; lidong@aircas.ac.cn; yanghong@aircas.ac.cn; panjie@aircas.ac.cn; xulq@aircas.ac.cn).

Wenmin Hu is with the National Joint Engineering Laboratory of Internet Applied Technology of Mines, China University of Mining and Technology, Xuzhou 221116, China (e-mail: huwm@cumt.edu.cn).

Jianguai Liu is with the Ottawa Research and Development Center, Agriculture and Agri-food Canada (AAFC), Ottawa K1A 0C6, Canada (e-mail: jianguai.liu@agr.gc.ca).

Yalin Liu is with the State key Laboratory of Rail Transit Engineering Information (FSDI), Xian 710043, China (e-mail: lynn6100@126.com).

Digital Object Identifier 10.1109/JSTARS.2021.3088263

lines and exposure points can be determined semi-automatically. Constant baseline and flight spacing are usually adopted for the whole photography region because effective Digital elevation model (DEM) data is lacking. Many manual adjustments are still needed to ensure enough overlap in rugged terrain. For example, some short flight lines in the high-terrain region are manually added to ensure an effective overlap.

With this traditional flight line planning approach, the desired sidelap and endlap cannot be guaranteed for the whole region of steep terrain, because if the highest terrain is used as reference to design the flight lines and camera exposure points, large redundancy and big overlap will be resulted in areas of lower terrain elevation. This process will not only cause a waste of flying resources, but also impact the triangulation accuracy or mapping accuracy as it is not the premium intersection geometry. So many efforts have been made to develop approaches using DEM in flight line planning [18], [19].

Fortunately, medium-resolution global DEM is now freely available from the Shuttle Radar Topographic Mission (SRTM) in 2001. Currently, the SRTM DEM dataset is one of the most complete and widely used DEM [20]. During the initial stage, 1 arc-second resolution data covering the USA and 3 arc-second resolution data for the globe were released, with unfilled gaps in high mountainous regions in Version-1 and Version-2. In 2013, the gap-filled SRTMGL3 Version-3.0 was released with a 3-arc-second resolution (90 m) for the globe [21]. The actual accuracy is that 90% absolute height errors are smaller than 9 m validated with groundtruth data collected globally [22]. The accuracy is precise enough for the flight quality assessment [23], and should be also sufficient for flight planning.

About 10 years ago, medium-resolution global DEM can be obtained freely from SRTM Version-2 or ASTER GDEM [24]. Some flight line planning software, such as Leica FPES [25], can load the DEM and calculate the average terrain elevation as the reference elevation, and then adjust the flight spacing and baseline automatically. But usually a constant flying height is used for the whole photography region and many manual adjusting work is also needed.

Now with the coming of 3D flight line planning era, commercial airborne system with the DEM-based flight line planning has become popular such as Leica MissionPro flight line planning software [16]. The state-of-the-art flight line planning software, such as IGI IGIplan and Topoflight Mission Planner, can change flight altitude according to terrain elevation in the steep or rugged terrain region, which can effectively reduce the number of flight lines, with the guarantee of a fine image resolution as well as adequate overlap at the same time [15], [26], [27]. However, their detailed algorithms are not disclosed.

We also developed a commercial flight management system FANS [28]. The FPS software is a subsystem of FANS which can support flight line planning of frame camera, line scan camera, LiDAR, and SAR where the SRTMGL3 DEM was used. It can provide four adaptable flight line planning modes using DEM data for frame camera, such as constant flight altitude for each flight line with constant baseline and flight spacing (Mode 1), constant flight altitude for each flight line with variable baseline and flight spacing (Mode 2), variable altitude for each flight line

with variable baseline and flight spacing (Mode 3), and variable altitude for each flight line segment with variable baseline and flight spacing to realize terrain following (Mode 4) where an innovative algorithm was used [29]. In Mode 4, the flight line segments can be adjusted by a fitting threshold and sample distance to precisely follow the terrain. To ensure the segments are consecutive, an appropriate weight value was set on the turning point for linear fitting.

Nowadays, the unmanned aircraft systems (UAS) take a huge market share for the aerial photography [30]–[32], and they are widely used for 3D reconstruction data capturing for disaster evaluation, cultural heritage protection, geological mapping, etc. [7], [33], [34].

However, current flight line planning and mapping tools for UAS are more focused on vendor-specific solutions and less focused on photographic properties [9]. Flight line planning systems usually are subordinate function of UAS ground station software [30], so some of them are still at low level for photography which usually use the fixed distance or fixed time interval triggering mode for image capturing. UAS has the advantage to fly with a terrain-following mode for its autopilot navigation and especially for the rotor drone. Now, UAS is also adopted for large-scale mapping applications with median-frame camera where the overlap and GSD is very sensitive to the terrain elevation. Thus, full automatic and high-quality flight line planning method is urgently needed. This article will disclose a professional piloted aircraft aerial photogrammetric survey flight line planning algorithm, in a hope to promote this procedure to improve the UAS-based photography application level.

II. METHODOLOGY OF FLIGHT LINE PLANNING

In actual project, the plane and camera performance should also be considered [3]. This article introduces the flight line planning method just from the geometric aspects. This section will introduce the common fundamentals of the calculations for adaptive flight line planning first, present its four modes and the top-level standardized flight line planning procedure, and then finally, disclose its sublevel key algorithms.

A. Fundamentals of the Calculations

1) *Flight Altitude, Baseline, and Flight Spacing*: For an airborne photography project, the first step is to determine the absolute flight altitude. The absolute flight altitude is calculated with GSD, camera parameters, and the reference terrain elevation. Because GSD is impacted by different terrain elevation, usually the average terrain elevation is used as the reference elevation to determine GSD, then absolute flight altitude H_a can be calculated as (1)

$$H_a = GSD/P_{size} * f + H_t \quad (1)$$

where P_{size} is the physical pixel size in the image sensor, and f is the focal length of camera, and H_t is the reference terrain elevation.

The baseline (B_X) is the distance between adjacent camera exposure points and the flight spacing (D_Y) is the distance

between adjacent flight lines. They can be calculated with the GSD, overlap, and image size as (2)

$$\begin{aligned} B_X &= GSD * N_x (1 - P_x) \\ D_Y &= GSD * N_y (1 - Q_y) \end{aligned} \quad (2)$$

where N_x is the image pixel number along the flight direction and N_y is the image pixel number across the flight direction. P_x is the endlap between photos along flight direction and Q_y is the sidelap between flight strips across flight direction.

In fact, because the ideal flat terrain does not exist, the photo ground coverage area will change with the terrain elevation, so the camera baseline and flight spacing should also be adjusted to keep a constant overlap in rugged terrain region.

2) *Ground Coverage of a Photo*: To adaptively design a flight line, the true ground coverage of each photo (also called footprint) is the most important factor which should be considered. The ground coordinate of an image point can be calculated using camera parameters, exterior orientation (EO) parameters, and DEM with a simple transformed collinearity equations as (3) for vertical photography:

$$\begin{aligned} X &= X_s + (Z - Z_s) \frac{x \cos k - y \sin k}{-f} \\ Y &= Y_s + (Z - Z_s) \frac{x \sin k + y \cos k}{-f} \end{aligned} \quad (3)$$

where the photo horizontal attitude is not used as it is exactly vertical photography during planning; X, Y, Z are the ground coordinates; X_s, Y_s, Z_s are the position elements of camera exposure station; x, y are the image coordinates; f is the focal length of the camera; k is the flight direction. Since ground coordinates X and Y are dependent on the actual ground elevation Z , the calculation is implemented by adopting an iterative procedure which can be found in [23].

The ground coordinates of all the edge pixels need to be derived to compute the ground coverage of a photo. To reduce processing time, the edge pixels are resampled at a given interval, and the ground coordinates of the resampled pixels are calculated to form the polygon boundaries of the photo ground coverage.

3) *Image Coordinate in Adjacent Photo*: Because the overlap should be represented in image space, the boundaries of a photos ground coverage should be projected into the image spaces of the adjacent photos in order to determine the overlap. This is conducted using the collinearity equations as (4)

$$\begin{aligned} x &= -f \frac{(X - X_s) \cos k - (Y - Y_s) \sin k}{Z - Z_s} \\ y &= -f \frac{(X - X_s) \sin k + (Y - Y_s) \cos k}{Z - Z_s}. \end{aligned} \quad (4)$$

Since $H_a = Z_s$, $H_t = Z$, and to simplify the equation, the X axis is rotated equal with the flight direction in the flight line planning coordinate system where the k is zero, so Eq. (4) can

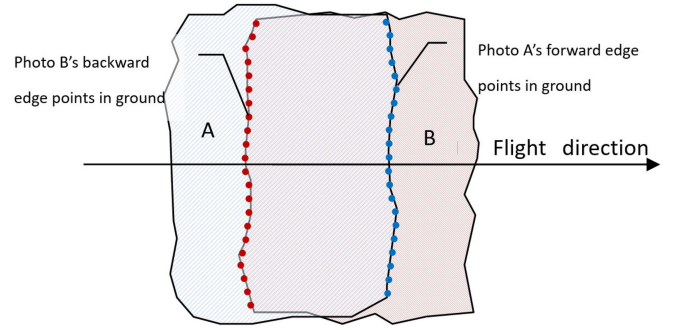


Fig. 1. Endlap relationship of stereo-pair on the ground.

be transformed as (5)

$$\begin{aligned} x &= -f \frac{X - X_s}{Z - Z_s} = -f \frac{X - X_s}{H_t - H_a} \\ y &= -f \frac{Y - Y_s}{Z - Z_s} = -f \frac{Y - Y_s}{H_t - H_a}. \end{aligned} \quad (5)$$

4) *The Endlap of a Stereo-Pair*: Sufficient endlap between stereo-pair photos is critical in frame image photogrammetry for subsequent data processing. If the endlap is too small, gaps can occur and mapping will fail. The endlap of photos is not a single value, but a range of values dependent on the terrain elevation and EO of the photos [23]. The minimum endlap is used as an indicator in flight line planning for it represents the worst overlap in stereo-pair photos. Fig. 1 shows the ground coverage of two successive photos A and B which can be derived using the procedure described in Section II-A.2. To calculate the forward overlap of photo A with photo B, the ground coordinates of the forward edge points of photo A are projected into the image space of photo B using (3). The minimum x of these points in photo B (x_{\min_BA}) in the along flight direction of the image space of photo B represents the worst forward endlap between the two photos. Similarly, the backward endlap of photo B with photo A is derived by projecting the ground coordinates of the backward edge points of photo B into the image space of photo A, and the maximum x of these points in photo A (x_{\max_AB}) represents the worst backward endlap between the two photos. Assuming that the origin of image coordinate for each photo is at its center, the minimum forward endlap of photo A with photo B ($P_{x_min_AB}$) and backward endlap of photo B with photo A ($P_{x_min_BA}$) are derived as (6) [23]

$$\begin{aligned} P_{x_min_AB} &= (l_x/2 + x_{\min_BA}) / l_x \\ P_{x_min_BA} &= (l_x/2 - x_{\max_AB}) / l_x \end{aligned} \quad (6)$$

where l_x is the physical size of the image along the flight direction. The smaller value of $P_{x_min_BA}$ and $P_{x_min_AB}$ is defined as the minimum endlap of the stereo-pair photo A and photo B.

5) *The Sidelap of Adjacent Flight Strips*: Sufficient sidelap is also necessary to ensure a successful aerial triangulation. The sidelap of a flight strip is defined as the minimum overlap with its adjacent flight strip in the image space. Fig. 2 illustrates the overlap of a flight strip with its adjacent flight strip in ground

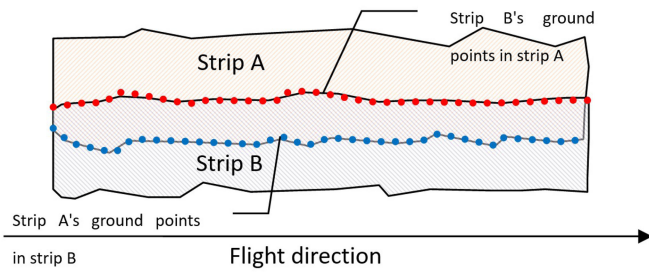


Fig. 2. Sidelap relationship of adjacent strips on the ground.

coordinate system. First, the ground coverage of flight line B is intersected with the ground coverage of the left flight line (strip A) to obtain the intersection points of strip B in strip A. These points are then projected into the image space of strip A. Their image coordinates can be calculated with (4). The maximum $y(y_{\max_BA})$ of the points represent the worst left sidelap of strip B. Similarly, the edge points of strip A can be projected into the image space in strip B, and the minimum $y(y_{\min_BA})$ represents the worst right sidelap of strip A. Assuming that the origin of image coordinate is at the photo center and the physical image size across the flight direction is l_y , the left sidelap ($Q_{y_min_BA}$) and right sidelap ($Q_{y_min_AB}$) are calculated as (7) [23]

$$\begin{aligned} Q_{y_min_BA} &= (l_y/2 - y_{\max_BA})/l_y \\ Q_{y_min_AB} &= (l_y/2 + y_{\min_AB})/l_y. \end{aligned} \quad (7)$$

The smaller value of $Q_{y_min_AB}$ and $Q_{y_min_BA}$ is defined as the minimum sidelap between strip A and strip B. The flight line position can be determined in accordance to the desired overlap between flight strips.

B. Adaptable Flight Line Planning

1) *Flight Line Planning Modes*: Different flight line planning strategies should be adopted for different terrain features. Flight line planning in the FANS FPS software can be categorized into four modes according to different strategies to determine flight altitude, flight spacing, and baseline.

Mode 1. Constant flight altitude for each flight line with constant baseline and flight spacing

This is the traditional method which uses the easiest strategy for flight line planning, as each flight line has the same flying altitude for the whole mission and the baseline between photos and the flight spacing between strips are fixed. DEM is only used to determine the average terrain elevation. This is suitable for flat terrain area. If it is used in a rugged terrain area, the designed overlap should be enlarged at the reference elevation to ensure sufficient overlap at the highest terrain.

Mode 2. Constant flight altitude for each flight line with variable baseline and flight spacing.

This is a common strategy for the flight line planning, where each flight line has the same flying altitude for the whole region, and the baseline and flight spacing are automatically adjusted by using a DEM to ensure the actual overlap meets the designed overlap for different terrain elevation.

Mode 3. Variable flight altitude for each flight line with variable baseline and flight spacing.

This is useful for mountainous region. The flights are horizontal at this mode while the flight altitude is changed between flights. Each absolute flight altitude is determined by the average terrain elevation of the nadir flight trajectory using the DEM data. Each flight line has different altitude to ensure the strip GSD is as stable as possible for different terrain elevation between flights. To decrease GSD variation, the flight direction is recommended to be adjusted according to the topography aspect.

Mode 4. Variable flight altitude along each flight line segment with variable baseline and flight spacing. This is an original terrain following mode in this article. In extreme rugged terrain region, each flight line is split by several consecutive segments to follow the terrain. The altitude of each segment is changed according to the terrain elevation. Each segment is not horizontal but with an inclined angle. This is the most complicated mode, with Mode 3 as a special case.

2) *Flight Line Planning Procedure*: The four flight line planning modes are implemented in a system with a unified planning procedure shown in Fig. 3 for a polygon region. The procedure consists of six main stages.

In Stage 1, given the geographic boundary of the region, the corresponding DEM can be automatically loaded to extract the average, highest, and lowest terrain elevation. The initial average flight spacing and camera baseline can be calculated with the reference average terrain elevation, the camera parameters, and plan parameters.

In Stage 2, the geographic coordinates of the polygon are transformed to the projection coordinate and flight direction should be designated according to topography aspect or project need. The flight line planning coordinate system should be rotated with the flight direction angle, and the flight line position can be determined just using its Y coordinate.

In Stage 3, based on the rotated coordinates of polygon corner points and average flight strip coverage, the Y coordinate of the first flight line can be calculated. Using the flight line Y to intersect with the polygon, the start point and the end point of the flight line can be acquired by extending an additional distance to guarantee sufficient border coverage. If the terrain-following mode (Mode 4) is used, the flight should be divided into several segments according to variation of terrain elevation. This will be detailed in Section II-B.3.

In Stage 4, with the start point of the flight line as first camera exposure point, successive exposure points can be derived adaptively using desired endlap as the constraint condition, which will be detailed in Section II-B.4. For Mode 1, iterative endlap calculation is not needed and exposure points were designed with a fixed baseline.

In Stage 5, the flight strip coverage and their image coordinates in the adjacent strip are calculated using the method described in Section II-A.5. The derived actual sidelap will be compared with the desired value. If the difference of the two is larger than a threshold, the flight position should be iteratively adjusted to bring the sidelap closer to the desired value. This procedure is detailed in Section II-B.5. For Mode 1, iterative

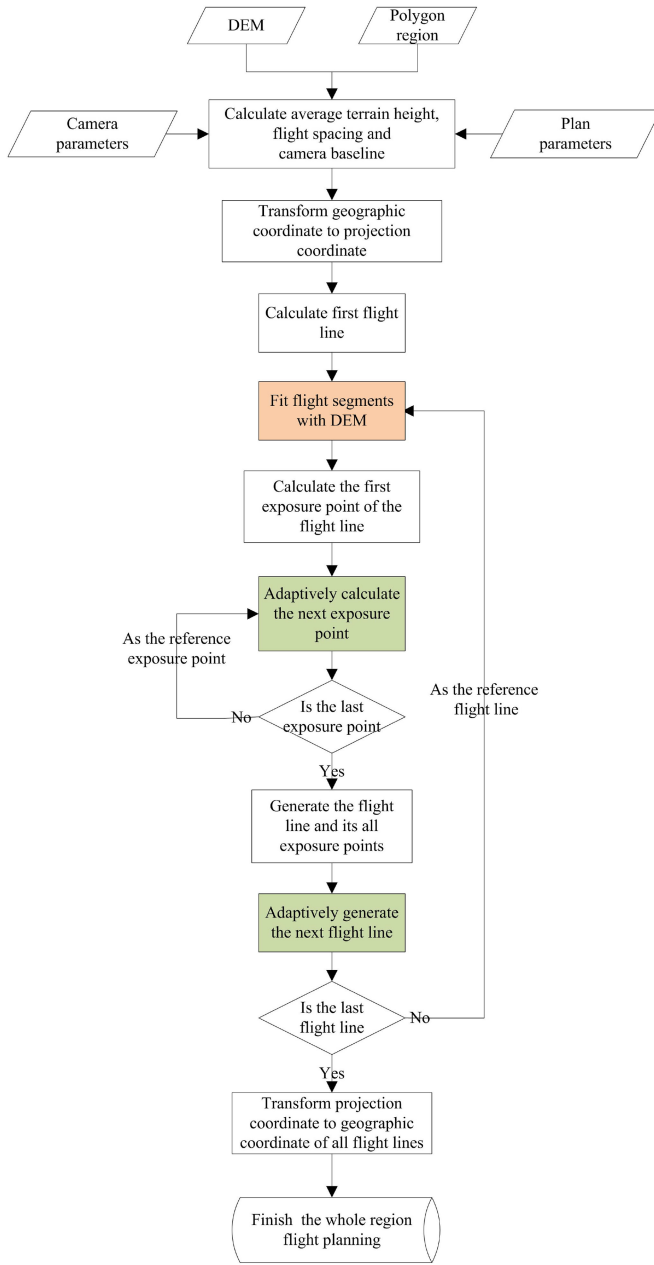


Fig. 3. Flight lines and exposure points calculation procedure.

sidelap calculation is not needed and flight lines were determined with a fixed flight spacing.

In Stage 6, the flight line planning is completed until the whole polygon region is covered with the flight strips. The obtained projection coordinates of the flight lines and exposure points are then transformed to geographic coordinates.

3) *Fit the Flight Line Segments With DEM*: For Mode 1 and Mode 2, there is no need to divide the whole flight line into different segments. For Mode 3, the flight line is sampled with a given ground distance interval to generate list of terrain points, and the corresponding air points can be acquired by adding a constant relative height (which is calculated with desired GSD and camera parameters). Then, the flight line altitude can be determined by the average altitude of the air points.

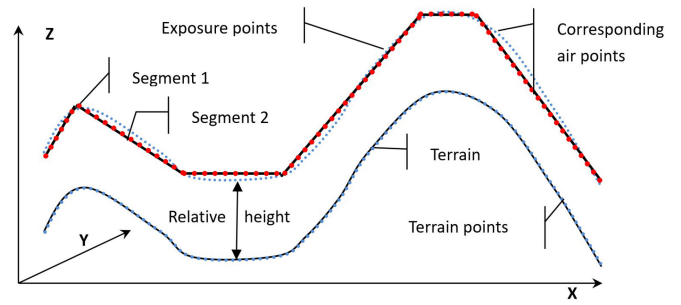


Fig. 4. Fitted segments in flight.

For Mode 4, the key procedure is to determine the flight line segments according to air point list, as it is difficult to navigate and fly based on the dense air points. The air points should be simplified and abstracted to form several segments in accordance with the terrain. This procedure is illustrated in Fig. 4. A linear fitting function is adopted to generate each segment. To simplify the calculation procedure, the coordinate system is rotated along with the flight direction. So the Y coordinate of the segments is the same in flight line. The straight line function of each flight line segment can be expressed as

$$Z = aX + b \quad (8)$$

where a is the slope coefficient and b is the intercept of the line segment.

The detailed linear fitting algorithm is described below, and the procedure is shown in Fig. 5.

In Step 1, generate the nadir terrain point list of the flight line with a given ground interval. The corresponding air point list is obtained by adding a constant relative height to the nadir terrain point list.

In Step 2, use the first two air points to generate a linear function, then a new point is added to fit a new linear function and the largest vertical distance of the three points to the new fitted line is derived. If it is larger than the threshold, the first two points form the first flight segment, otherwise the fourth point is added and the four points are used to fit a new linear function. The above procedure is repeated until the largest vertical distance of the points in the linear fit procedure is bigger than the threshold. Then the first segment is determined. The threshold can be determined by the project parameters; for example, $1/5$ relative flying height. If the threshold is smaller, more segments will be generated and better GSD can be achieved.

In Step 3, once the first segment is determined, Step 2 is repeated to generate subsequent segments, using the end point of the previous segment as the first point. To ensure the segments are consecutive, an appropriate weight value is set for the end point of the previous segment.

4) *Adaptively Generate Camera Exposure Points*: Sufficient endlap is an important criteria for the frame camera stereo-pairs mapping. It should be planned with DEM to ensure it is big enough for the subsequent data process. If the endlap is too small, it will conduct in missing overlap between stereo-pairs which will result in data gap for mapping. This is the most serious aerial photography fault.

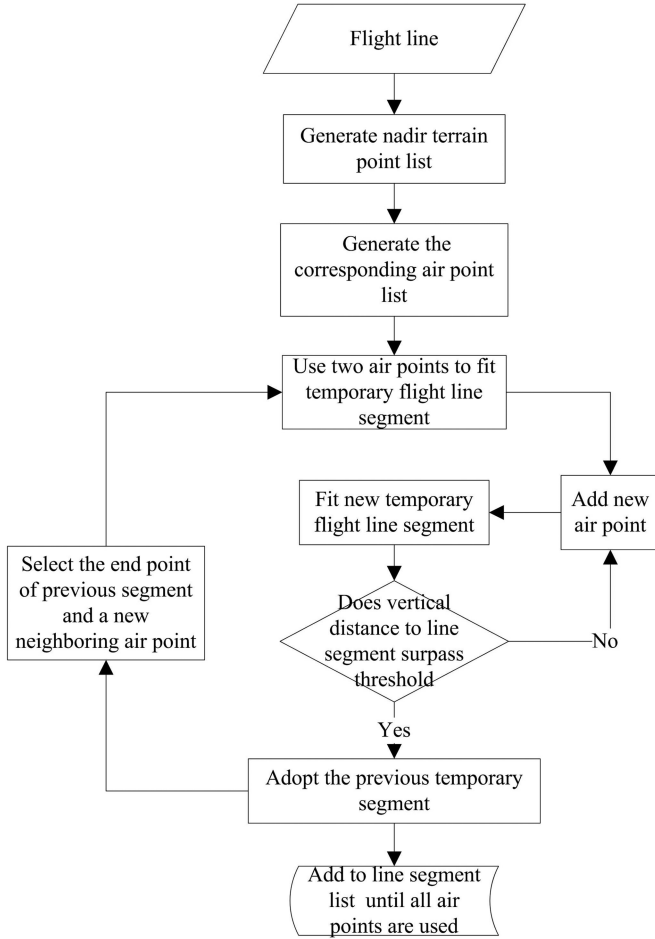


Fig. 5. Fitting flight line segments procedure.

When the flight line coordinate Y is determined, the start and end points of the flight line can be determined by intersecting with the region polygon, and the exposure points in the line can be calculated successively. First, the start point of the flight line can be seen as the first exposure point. Then, the first exposure point X was added a camera baseline length to generate the initial second exposure point coordinate X_2 as (9).

$$X_2 = X_1 + L_X (1 - P_x) \quad (9)$$

where L_X is the width of photo ground coverage along the flight direction on the reference terrain elevation, which can be calculated as $GSD * N_x$. The second photo footprint can be calculated respectively using algorithm described in Section II-A.2, and the actual new endlap $P_{x_{new}}$ can be calculated with (6) in Section II-A.4 based on the EO parameters of stereo-pair and DEM data. The highest terrain elevation can also be acquired with the points of second footprint, where it represents the minimum overlap location. The new footprint width along the flight direction can be calculated with (10)

$$L_{X_{new}} = (H_a - H_{t_{max}}) / f * l_x \quad (10)$$

where H_a is the absolute reference camera exposure point altitude. $H_{t_{max}}$ is the highest terrain elevation of temporary

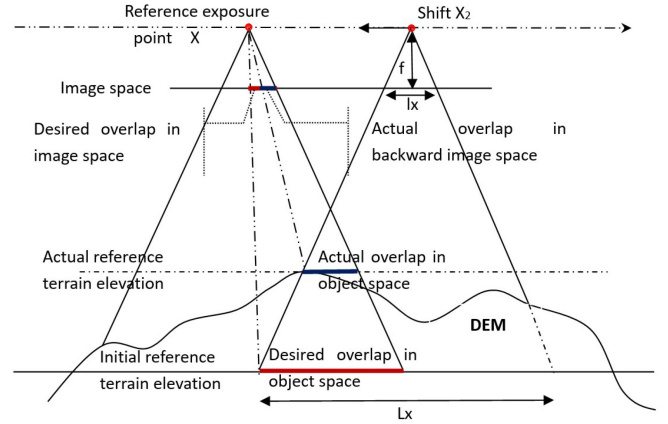


Fig. 6. Endlap relationship in stereo-pair.

second footprint backward edge ground points, which represent the poorest backward overlap in the stereo-pair photos.

The backward endlap in stereo-pair is illustrated in Fig. 6. The forward endlap can be calculated similarly in the forward image space. The smaller value of them is defined as the endlap of stereo-pair images.

The final $X_{2_{new}}$ which represents the final second exposure point location can be determined by iteratively adjusting the X_2 with (11) until the endlap difference ($P_{x_{new}} - P_x$) is small enough than threshold value which can be commonly set as 1%–5%. Then, all the other exposure points in the flight line can be calculated by repeating up-context procedure as Fig. 7.

$$X_{2_{new}} = X_2 + L_{X_{new}} (P_{x_{new}} - P_x). \quad (11)$$

5) *Adaptively Calculate Flight Lines:* Flight line Y position is derived using flight strip sidelap. Sufficient sidelap is necessary to ensure that the photography area has a strong geometry which enables successful triangulation and bundle adjustment. If the sidelap is not big enough, it will lead to low accuracy or data mapping gaps.

To calculate the sidelap, the flight strip coverage should be calculated first. The first flight line of the region can be determined with the flight direction, initial strip coverage width, and side extend scale which ensure redundancy to cover the region. Usually, s is smaller than 0.5. Then, the first flight line Y_1 coordinate can be obtained as (12) with Y_{min} , the minimum value of the region polygon corner points.

$$Y_1 = Y_{min} + L_Y / 2 - s * L_Y \quad (12)$$

where L_Y is the width of strip coverage on the ground across the flight direction on the reference terrain elevation, which can be calculated as $GSD * N_y$. The Y_1 horizontal line can be used to intersect with the polygon, where the start point and end point can be generated by pulsing an extending distance along flight direction to the intersection points to ensure sufficient border coverage. Once the first flight line is determined with its start and end points, the flight segments can be determined with the method described in Section II-B.3 if Mode 4 is adopted.

The second flight line initial Y_2 can be obtained by adding a constant flight spacing to Y_1 according to (13). With Y_2 line

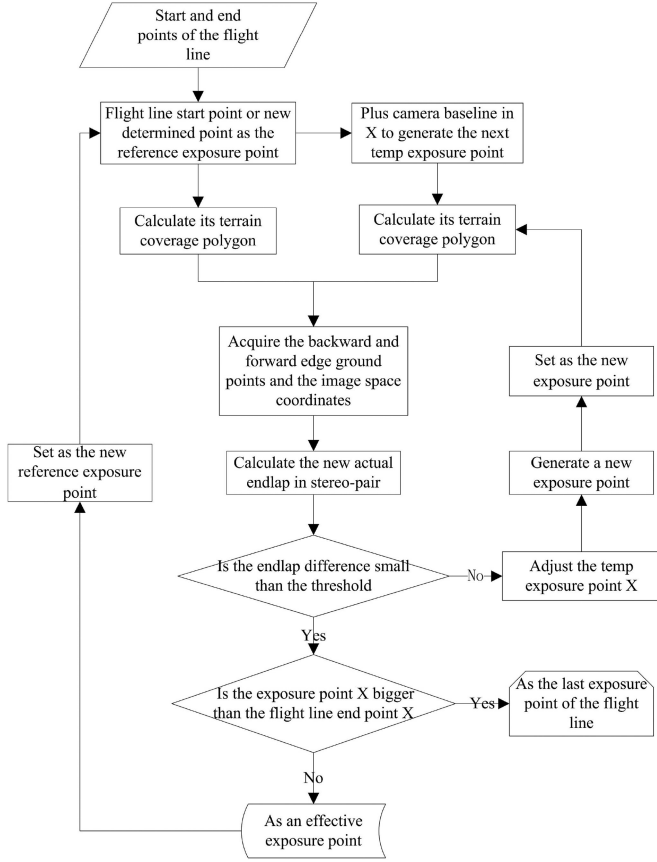


Fig. 7. Camera exposure points calculation procedure.

intersect with the region polygon, the start and end points of the second flight line can be determined. Similarly, the flight segments should be calculated with the algorithm of Section II-B.3 if Mode 4 is adopted.

$$Y_2 = Y_1 + L_Y (1 - Q_y). \quad (13)$$

To verify the actual sidelap with the initial Y_2 flight line, the flight strip coverage should be calculated to derive the overlap. Flight strip coverage is the union of all the photos coverage in the flight. To simplify the strip coverage calculation procedure, the frame photos strip coverage is assumed to be the same as that of an equivalent line scanner camera. With this simplification, the first and second flight strip coverages can be calculated, respectively. The new actual sidelap Q_{y_new} can be calculated with the sidelap calculation procedure in Section II-A.5 with (7).

Because, usually the max terrain elevation position of the strip coverage boundary represents the poorest overlap, the max terrain elevation was used to determine the new strip coverage width $L_{Y_{new}}$

$$L_{Y_{new}} = (H_a - H_{t_{max}}) / f * l_y \quad (14)$$

where $H_{t_{max}}$ is the max terrain elevation of the strip coverage boundary. If the difference between $Q_{y_{new}}$ and Q_y is larger than the overlap threshold which is commonly set as 1%–5%, the new second flight $Y_{2_{new}}$ should be adjusted using (15)

$$Y_{2_{new}} = Y_2 + L_{Y_{new}} (Q_{y_{new}} - Q_y). \quad (15)$$

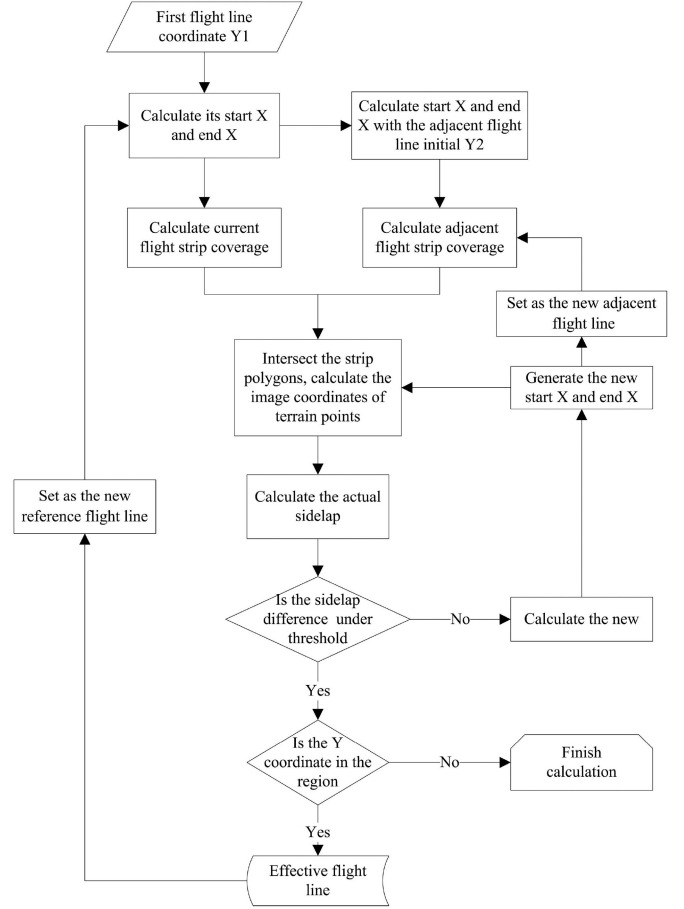


Fig. 8. Flight line calculation procedure.

The final $Y_{2_{new}}$ can be adopted while the value of $(Q_{y_{new}} - Q_y)$ is small enough under the threshold with the iteration procedure. Similarly, the third flight line can be determined based on the second flight line. All the other flight lines can be generated until the last flight line Y is bigger than the max Y of the region polygon. The detailed adaptive flight line calculation procedure is depicted in Fig. 8.

III. TEST AND VALIDATION

A. Hypothetical Test Comparisons

1) *Test Scenarios*: To assess the flight line planning quality, a hypothetical test in a polygon region which contains both steep and plain terrain was adopted to implement the four flight line planning modes. Their flight line field workload was compared, and the GSD was analyzed. Their flight line planning overlap results were analyzed which were generated with the flight evaluation system software package method as detailed in [23].

The region locates in Shandong province, China, which contains the famous Mount Tai. The highest terrain elevation is about 1517 m and the lowest is about 47 m. The Leica's most advanced DMC-III frame camera was used as the reference camera [35]. The detailed project parameters for this test are listed in Table I.

2) *Comparison of Project Workload*: The four flight line planning modes were tested. For Mode 1, to ensure sufficient

TABLE I
PROJECT PARAMETERS FOR THE REGION

Parameters	Values
Type of terrain	Mountain
Average terrain elevation	305 m
Highest terrain elevation	1517 m
Lowest terrain elevation	47 m
Region	Center coordinate
	E117.08039° N36.34632°
	Area
	2056 km ²
Camera	DMC-III
Focal length	92 mm
Pixel size	3.9 μ m
Image size	25728*14592
Desired GSD	20 cm
Desired relative flying height	4718 m
Flight direction	West-East
DEM	SRTMGL3

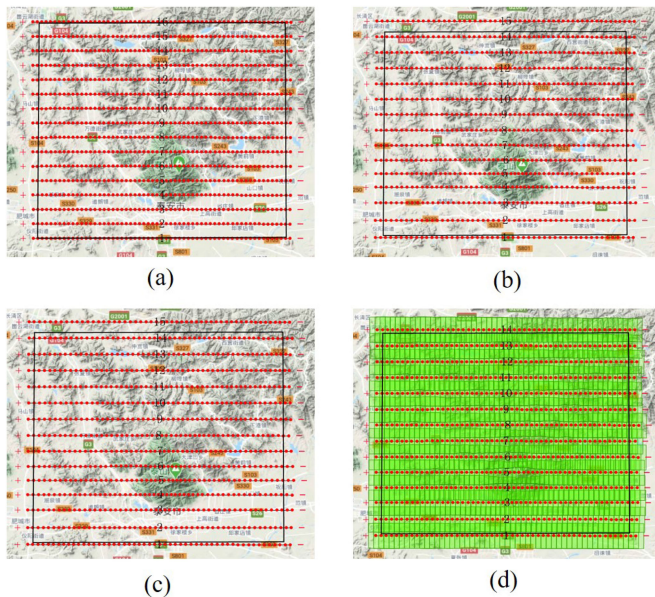


Fig. 9. Screen shots for the four flight line planning modes. (a) Mode 1 planning result. (b) Mode 2 planning result. (c) Mode 3 planning result. (d) Mode 4 planning result.

photo overlap at areas with the highest elevation, a big overlap is used with the endlap 70% and sidelap 45% at the reference average terrain elevation for the whole region with a fixed baseline and flight spacing. Eventually, 16 flight lines and 944 camera exposure points were generated. For Mode 2, with a variable baseline, flight spacing, and a constant flight altitude, 15 flight lines and 802 camera exposure points were generated. For Mode 3, with the variable baseline, flight spacing, and flight altitude, 15 flight lines and 796 camera exposure points were generated. For Mode 4, with the terrain-following strategy, the sampled ground interval is 100 m and the fitting threshold distance is set to 200 m in vertical direction, and 14 flight lines and 743 camera exposure points were generated. The flight planning calculation efficiency is very high and each mode can be finished in several minutes. The Google topographic map was used as the background in the FANS-FPS software. Screen snapshots of all the four modes flight line planning are shown in Fig. 9.

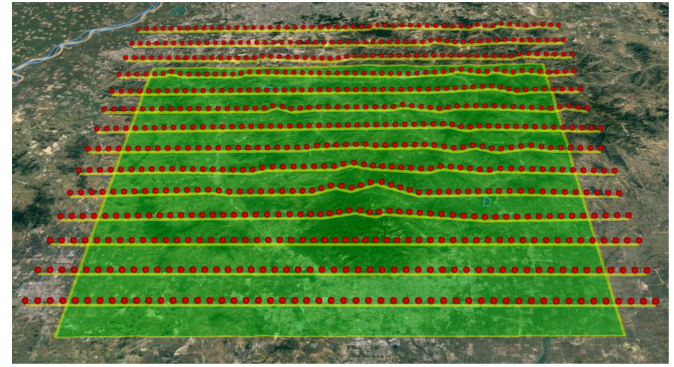


Fig. 10. Flight line planning result of Mode 4 displayed in Google Earth.

The flight line planning result for Mode 4 was also exported with *.kml format, and shown in Google Earth to illustrate the terrain-following effect (Fig. 10).

Fig. 10 indicates that the flight line is separated with several segments to follow the terrain on the high mountain subregion.

As a summary, the statistics of results from different flight line planning modes are given in Table II.

From Figs. 9 and 10 and Table II, it is clear that Mode 1 is not efficient as more flight lines and photos are needed to complete the mission. In Modes 2 and 3, the flight spacing and camera exposure points are adjusted according to terrain elevation and high terrain regions have denser exposure points than the low terrain region. The change of the variable baseline is not obvious in this test as the relative flying height is much higher than the change in terrain elevation. If a higher resolution GSD is used, the flight spacing and baseline will change obviously. Mode 4 is the most efficient method in terms of flight lines and camera exposure points; however, it needs more sophisticated flying and navigation techniques.

3) *Comparison of Flight Line Planning Quality*: To inspect the flight line planning result, the flight quality assessment using geometric calculation method as provided in [23] was used. The flight line planning result was exported as a standard EO format, in which the attitudes (ω , ϕ , κ) are set to 0,0, flight direction, respectively. With the EO data, four adjacent overlaps (forward endlap, backward endlap, left sidelap, and right sidelap) were calculated and exported for each photo. The forward endlap and backward endlap are combined as endlap, left sidelap, and right sidelap are combined as sidelap. The overlap results of the four modes are illustrated using histograms in Fig. 11.

From Fig. 11, overlap of Mode 1 changes widely and cannot retain an ideal overlap for the whole region, where the minimum endlap is about 59.8% and the largest is about 71.4%, the minimum sidelap is about 27.7% and largest is about 47.5%. Modes 2, 3, and 4 have narrow overlap distribution, which can ensure that the minimum sidelaps and endlaps are quite close to the desired value where the overlap difference threshold is set to 1% in FANS-FPS software.

To analyze the image GSD, the image was sampled with 1000 pixels per step, GSD of the sample points can be calculated with collinear equation with DEM, and all the GSD samples of

TABLE II
COMPARISON FOR PROJECT WORKLOAD OF DIFFERENT FLIGHT LINE PLANNING MODES

Mode	Flight lines	Camera exposure points	Total flight lines length(km)	Max GSD (m)	Min GSD (m)	Absolute flight altitude(m)	Reference Terrain elevation(m)	Designated overlap at reference(Endlap,Sidelap)
Mode1	16	944	812	0.21	0.15	5023	305	45%,70%
Mode2	15	802	776	0.21	0.15	5023	305	30%,65%
Mode3	15	796	769	0.21	0.15	4870-5103	Nadir terrain	30%,65%
Mode4	14	743	743	0.21	0.17	4680-6274	Nadir terrain	30%,65%

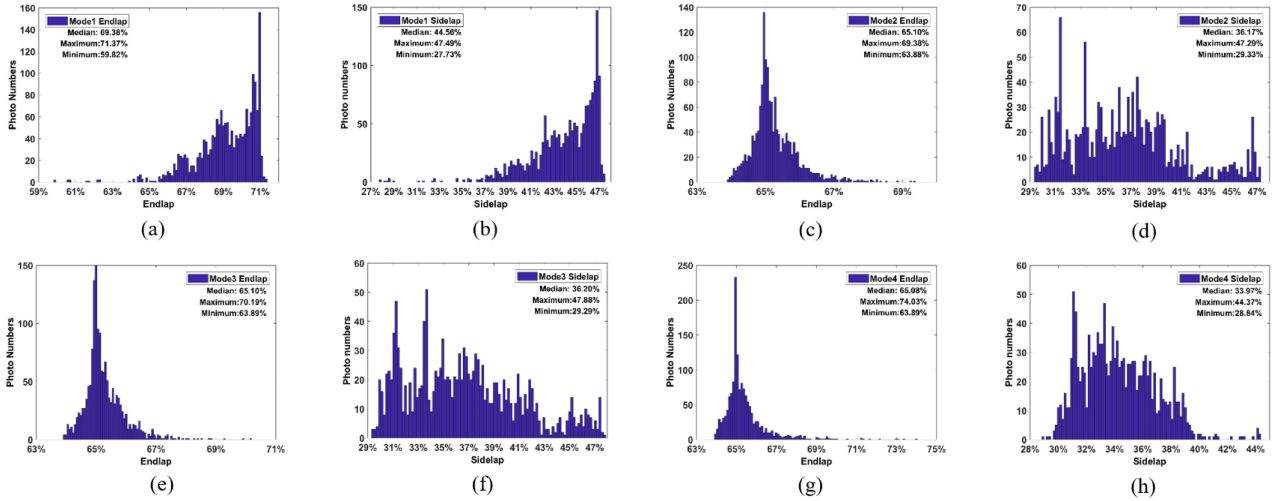


Fig. 11. Overlap results of four modes. (a) Mode 1 endlap. (b) Mode 1 sidelap. (c) Mode 2 endlap. (d) Mode 2 sidelap. (e) Mode 3 endlap. (f) Mode 3 sidelap. (g) Mode 4 endlap. (h) Mode 4 sidelap.

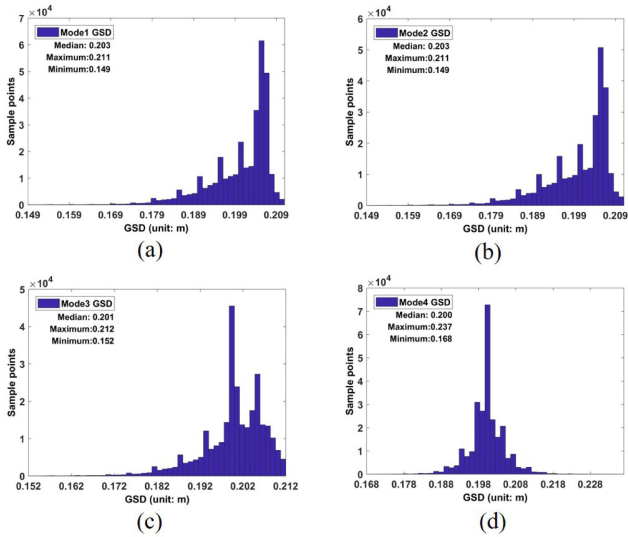


Fig. 12. GSD distribution of 4 modes. (a) Mode 1 GSD distribution. (b) Mode 2 GSD distribution. (c) Mode 3 GSD distribution. (d) Mode 4 GSD distribution.

the images were exported for the whole region. The statistics of GSD for the four modes are shown in Fig. 12.

Fig. 12 shows that Mode 1 and Mode 2 have similar GSD distribution, because of the same flight altitude. Mode 3 has a better GSD distribution than Mode 1 and Mode 2, for GSDs are much more closer to the desired value. GSD in Mode 4 is more stable and almost has a normal distribution due to terrain following flight. The GSD distributions in the four modes did

not change obviously, for the fly altitude is much higher than terrain elevation difference. With a higher resolution, the GSD difference will be more apparent.

The overlap histogram indicate that, a flight mission with variable flight parameters produce better performance in overlap. Similarly, the GSD histogram indicate that, better distribution of GSD is achieved with variable altitude parameters. Although Mode 4 increases the difficulty and risk of flying, it is optimal for overlap and GSD, and may be widely adopted for UAS platform for high-resolution data acquisition. Mode 2 and Mode 3 are still popular approaches for flight line planning nowadays on piloted aircraft platform.

B. Actual Project Validation

1) *Project Introduction:* The FANS-FPS was also used in an infrastructure project in a high mountainous area located in Tibet province of China. The oblique camera AMC5100 and Rigel LiDAR were used to acquire data simultaneously where the flight line planning Mode 3 was used. The AMC5100 oblique camera system consists of five PhaseOne iXU-RS1000 cameras. The detailed project parameters are listed in Table III.

Based on the project need, desired GSD was 5 cm. Since the maximum terrain elevation difference is about 1200 m, larger than the desired relative flying height (761 m), Mode 3 is adopted to plan flights to ensure the flying safety and more stable GSD. Many additional camera exposure points were added along flight direction to acquire multiview images for 3D reality construction of the region. The absolute flight altitude is calculated as the sum

TABLE III
PROJECT PARAMETERS FOR THE TIBET PROJECT REGION

Parameters	Values
Type of terrain	High Mountain
Average terrain elevation	3597 m
Highest terrain elevation	4218 m
Lowest terrain elevation	3037 m
Region	Center Coordinate
	N30.46179° E96.66965°
	Area
	4.5 km ²
Camera	AMC5100
Desired GSD(Nadir camera)	5 cm
Focal length(Nadir camera)	70 mm
Image size	11608*8708
Pixel size	4.6 μ m
Desired relative flying height	761 m
Desired sidelap(Nadir camera)	40%
Desired endlap(Nadir camera)	75%
DEM	SRTMGL3 AS350
Platform	Helicopter

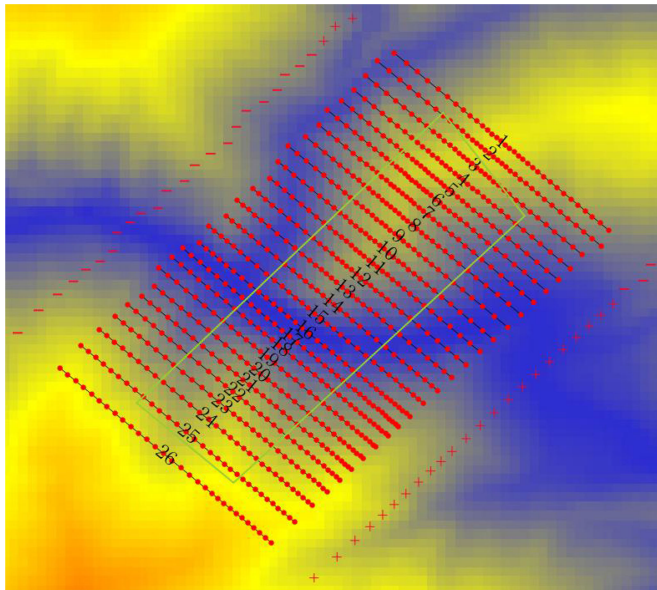


Fig. 13. Planning result for AMC5100 camera.

of the desired relative flying height and the average flight nadir terrain elevation. Eventually, the designed absolute flight altitude was changed from 3957 to 4991 m. The flight line planning result is shown in Fig. 13 by FANS-FPS software and it can also be exported and displayed in Google Earth as Fig. 14.

Figs. 13 and 14 show that the baseline between photos changed obviously in according to elevation as it has high resolution and low relative flying height compared to the Mount Tai test. The relative flying height is the main reason for the overlap change in high mountainous area. For low relative flying height, the overlap changes with terrain substantially. In conclusion, for high-resolution data acquisition with a low relative flying height, changing flight altitude is important to achieve more constant GSD and desired overlap.

2) *Project Result*: To analyze the planning quality, GSDs of each photo sample points were calculated with the same method in Section III-A.3. From the distribution as shown in

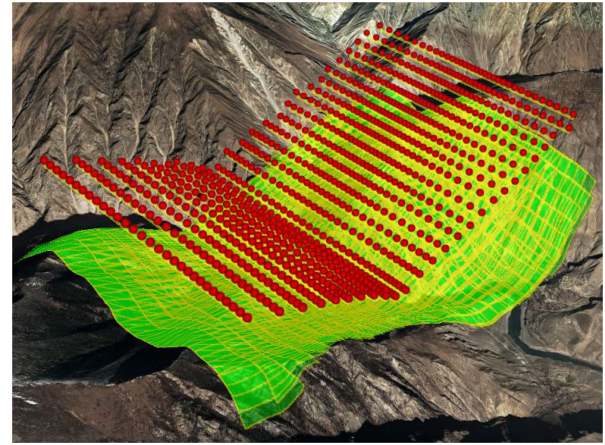


Fig. 14. Flight line planning result displayed in Google Earth.

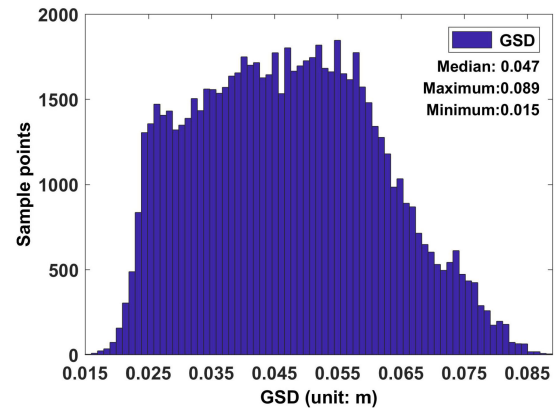


Fig. 16. Theoretical GSD distribution.

Fig. 13, GSDs of Mode 3 have a symmetrical and centralized distribution, which will ensure an ideal mapping result.

After the data acquisition, the nadir camera images were used to generate ortho-image with the Context Capture software, and the GSD report was finally reported in Fig. 15. It is observed that, most GSD values are between 3 and 7 cm, which are consistent with Fig. 16. The results show that the Mode 3 flight line planning method is effective.

Finally, all the nadir and oblique camera data were processed with the Context Capture to generate the 3D product. Fig. 17 shows the reality 3D model in the whole region and Fig. 18 shows a part of the valley.

In Fig. 18, it shows a very distinct 3D reality model of the valley. This proves that Mode 3 flight line planning method provides an effective approach to ensure the constant high-resolution image in high mountainous region, and high accuracy support in such low-valley subregion.

C. Potential Errors Analysis

1) *Planning Aroused Errors*: As well known, the flight line planning errors consist of the overlap error and the GSD error, which are aroused by the DEM error. The SRTMGL3 DEM was adopted considering flight line planning efficiency and

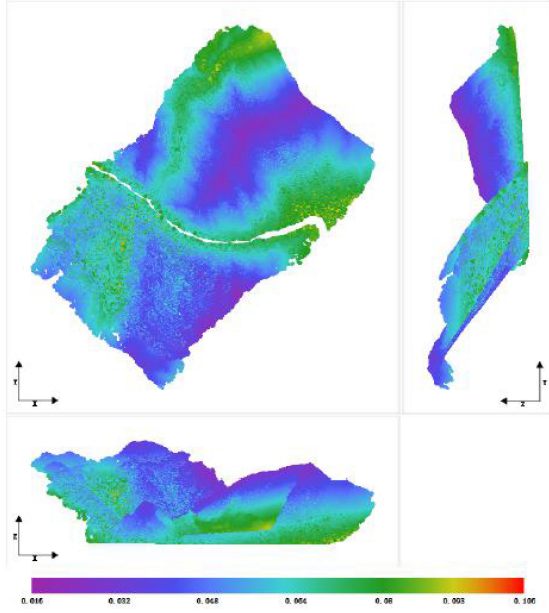


Fig. 15. Actual GSD distribution of the project (from Context Capture report).

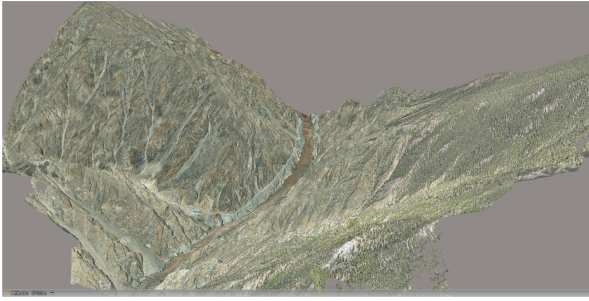


Fig. 17. Whole reality 3D result of the project.



Fig. 18. High-resolution reality 3D model of the valley.

precision in FANS FPS. The overlap error is determined by the relative flight height and the DEM elevation error, which can be expressed with (15) in [23].

$$\begin{aligned} RMSE_{\text{endlap}} &\approx \frac{\sqrt{2}}{2} \cdot \frac{RMSE_Z}{\bar{Z}} \\ RMSE_{\text{sidelap}} &\approx \frac{\sqrt{2}}{2} \cdot \frac{RMSE_Z}{\bar{Z}} \end{aligned} \quad (16)$$

The accuracy of SRTMGL3 DEM is that 90% absolute height errors are smaller than 9 m validated with groundtruth data

collected globally [22]. For a 10-m RMSE of SRTMGL3 DEM (the assumption has enlarged the error) and 761 m relative flying height in the above test, the overlap error is about 0.9% ($\frac{\sqrt{2}}{2} \cdot 10/761$), much smaller compared with the overlap. It is obvious that GSD is impacted by the DEM error, relative flying height and camera parameters. For example, the GSD variation can be expressed with 10/761 (1.3%) for 10-m RMSE of the DEM and 761-m relative height in the above high-resolution test. The GSD variation is very small, so the DEM error can be ignored for GSD calculation.

2) *Flying Induced Errors*: In a flight mission, the actual camera pointing angle and flying deviation of the desired flight line will impact the final overlap and GSD. Fortunately, the gyro stabilization mount was widely used to keep the desired camera pointing angle, which can keep 0.3° residual deviation from perpendicular for typical standalone mode [36]. For example, the induced overlap deviation can be calculated with $0.3/40$ (0.75%) for a 40 FOV (field of view) camera which is very small and can be ignored.

Usually, horizontal flight deviation is smaller than 50 m for typical mission with manned-pilot plane, and is smaller than 10 m for auto-pilot mode for most projects. Sidelap deviation can be expressed with $50/11608 \times 0.05$ in the above high-resolution project. It is about 8.6%, so the flying deviation impacts the image overlap seriously.

Fine flight line planning is a initial condition for the aerial data capturing. The camera exposure interval, flying deviation, gyro stabilization mount precision, and positioning precision of camera trigger in field flying are also important factors for final image overlap quality.

IV. SUMMARY

This article presented an adaptable flight line planning approach with which the flight lines and camera exposure points can be planned automatically with the overlap and GSD constraint by using the DEM data. Details of the algorithms are described and the planning results are assessed.

It can be concluded that, Mode 1, using a constant baseline and flight spacing, is useful for flat terrain, but not for rugged terrain. Mode 2, with constant altitude for the whole region but variable baseline and flight spacing, is the mainstream flight line planning method currently. It can fulfill the requirements for most projects. Mode 3 is very useful in high rugged terrain region as it can take account of both GSD and flying safety factors and it is better to design the flight direction along with the terrain forms trend to decrease the terrain elevation variation in flight line. This method may be a mainstream method in the future. The terrain following Mode 4 is the best way in terms of GSD and total flight workload; however, it is difficult for actual field flight using piloted aircraft platforms and it would be used more on UAS platform for high-resolution data acquisition. In actual project, the plane and camera performance must also be considered. The flight line planning result must match with them. The method of this article is not only for frame camera, but also useful for line scan camera or LiDAR where it does not need to calculate camera exposure points. The algorithm is derived for vertical photography, but the improved algorithm should also be effective

for oblique photography, and even each photo can be planned to have a unique oblique angle which is perpendicular to the ground surface to realize optimal GSD and imaging quality. In the natural resource geophysical prospecting as magnetic force measuring, it also needs terrain-following flight because of its high sensitivity to the relative flying height. Thus, Mode 4 should be useful for the demand.

ACKNOWLEDGMENT

The authors would like to acknowledge the State key Laboratory of Rail Transit Engineering Information for sharing their experiment data.

REFERENCES

- [1] X. Wu, D. Hong, J. Tian, J. Chanussot, W. Li, and R. Tao, "ORSIm detector: A novel object detection framework in optical remote sensing imagery using spatial-frequency channel features," *IEEE Trans. Geosci. Remote Sens.*, vol. 57, no. 7, pp. 5146–5158, Jul. 2019.
- [2] D. Hong, L. Gao, J. Yao, B. Zhang, A. Plaza, and J. Chanussot, "Graph convolutional networks for hyperspectral image classification," *IEEE Trans. Geosci. Remote Sens.*, early access, 2020, doi: [10.1109/TGRS.2020.3015157](https://doi.org/10.1109/TGRS.2020.3015157).
- [3] D. Hong *et al.*, "More diverse means better: Multimodal deep learning meets remote-sensing imagery classification," *IEEE Trans. Geosci. Remote Sens.*, vol. 59, no. 5, pp. 4340–4354, May 2021.
- [4] D. Hong, N. Yokoya, G.-S. Xia, J. Chanussot, and X. X. Zhu, "X-modalNet: A semi-supervised deep cross-modal network for classification of remote sensing data," *ISPRS J. Photogramm. Remote Sens.*, vol. 167, pp. 12–23, 2020.
- [5] M. Pepe, L. Fregonese, and M. Scaioni, "Planning airborne photogrammetry and remote-sensing missions with modern platforms and sensors," *Eur. J. Remote Sens.*, vol. 51, no. 1, pp. 412–436, 2018.
- [6] H. Zhao, B. Cui, and G. Jia, "A flight direction design method for airborne spectral imaging considering the anisotropy reflectance of the target in rugged terrain," *Sensors*, vol. 19, no. 12, 2019, Art. no. 2715.
- [7] F. Chiabrando, A. Lingua, P. Maschio, and L. T. Losè, "The influence of flight planning and camera orientation in UAVs photogrammetry. A test in the area of Rocca San Silvestro (LI), Tuscany," *Int. Arch. Photogramm. Remote Sens. Spatial Inf. Sci.*, vol. 42, p. 163–170, 2017. [Online]. Available: <https://doi.org/10.5194/isprs-archives-XLII-2-W3-163-2017>
- [8] J. P. Dandois, M. Olano, and E. C. Ellis, "Optimal altitude, overlap, and weather conditions for computer vision UAV estimates of forest structure," *Remote Sens.*, vol. 7, no. 10, pp. 13895–13920, 2015.
- [9] L. Roth, A. Hund, and H. Aasen, "Phenofly planning tool: Flight planning for high-resolution optical remote sensing with unmanned areal systems," *Plant Methods*, vol. 14, no. 116, 2018. [Online]. Available: <https://doi.org/10.1186/s13007-018-0376-6>
- [10] Y.-H. Tu, S. Phinn, K. Johansen, A. Robson, and D. Wu, "Optimising drone flight planning for measuring horticultural tree crop structure," *ISPRS J. Photogramm. Remote Sens.*, vol. 160, pp. 83–96, 2020.
- [11] A. Manconi, M. Ziegler, T. Blöchliger, and A. Wolter, "Optimization of unmanned aerial vehicles flight planning in steep terrains," *Int. J. Remote Sens.*, vol. 40, no. 7, pp. 2483–2492, 2019.
- [12] K. Kozmus Trajkovski, D. Grigillo, and D. Petrovič, "Optimization of UAV flight missions in steep terrain," *Remote Sens.*, vol. 12, no. 8, 2020, Art. no. 1293.
- [13] K. Kraus, *Photogrammetry: Geometry From Images and Laser Scans*. Walter de Gruyter, 2011.
- [14] Leica-Geosystems, "Leica MissionPro flight planning software," Accessed: 5 May, 2020. [Online]. Available: <https://leica-geosystems.com/products/airborne-systems/software/leica-missionpro>
- [15] IGI, "IGIplan state-of-the-art mission planning software," [EB/OL], Accessed: 5 May, 2020. [Online]. Available: <https://www.igi-systems.com/files/IGI/Brochures/IGIplan/IGIplan.pdf>.
- [16] Leica-Geosystems, "Leica ASCOT (aerial survey control tool)," [EB/OL], Accessed: 5 May, 2020. [Online]. Available: https://w3.leica-geosystems.com/downloads/123/zz/airborne/ascot/brochures/ASCOT_brochure.pdf.
- [17] TrackAir, "X-Track flight management system software," Accessed 20 May, 2020. [Online]. Available: <http://www.trackair.com/manuals/Track%20X-TRACK%20snapPLAN%20manual.pdf>
- [18] Y.-W. Fan, J.-Y. Gong, C.-G. Tan, and R.-Y. Wang, "Research on computer-assisted DEM-based flight plan of aerial photography," in *Proc. First Int. Conf. Intell. Netw. Intell. Syst.*, 2008, pp. 470–474.
- [19] W. Zhu and R. H. Yan, "A DEM-based approach of technical project aerial photography," *Science of Surveying and Mapping*, vol. 27, pp. 42–46, 2002.
- [20] Y. Su and Q. Guo, "A practical method for SRTM DEM correction over vegetated mountain areas," *ISPRS J. Photogramm. Remote Sens.*, vol. 87, pp. 216–228, 2014.
- [21] NASA, "NASA shuttle radar topography mission Global 1 arc second. NASA LP DAAC," [EB/OL], [Online]. Accessed: Feb. 28, 2017. [Online]. Available: https://lpdaac.usgs.gov/dataset_discovery/measures/measures_products_table/srtmg11_v003
- [22] E. Rodriguez, C. S. Morris, and J. E. Belz, "A global assessment of the SRTM performance," *Photogramm. Eng. Remote Sens.*, vol. 72, no. 3, pp. 249–260, 2006.
- [23] H. Zhao *et al.*, "Aerial photography flight quality assessment with GPS/INS and DEM data," *ISPRS J. Photogramm. Remote Sens.*, vol. 135, pp. 60–73, 2018.
- [24] T. Tachikawa, M. Hato, M. Kaku, and A. Iwasaki, "Characteristics of ASTER GDEM version 2," in *Proc. IEEE Int. Geosci. Remote Sens. Symp.*, 2011, pp. 3657–3660.
- [25] Leica-Geosystems, "Leica FPES flight planning and evaluation software," [EB/OL], Accessed: 27 May, 2020. [Online]. Available: https://w3.leica-geosystems.com/downloads/123/zz/airborne/fpes/brochures/Leica_FPES_BRO.pdf.
- [26] M. Möllney and J. Kremer, "Contour flying for airborne data acquisition," *Photogramm. Week*, vol. 13, pp. 117–129, 2013.
- [27] TopoFlight, "TopoFlight mission planner," [EB/OL], Accessed: 5 May, 2020. [Online]. Available: <https://www.topoflight.com/products/topoflight-mission-planner/>.
- [28] FANS, "FANS-FMS make your flight easier," [EB/OL], Accessed: 1 May, 2020. [Online]. Available: <https://www.fansfms.com/>.
- [29] H. Zhao *et al.*, "Non-horizontal route planning method based on terrain elevation, terminal and storage medium," China Patent ZL201 711 039 413.0.
- [30] I. Colomina and P. Molina, "Unmanned aerial systems for photogramm. and remote sensing: A review," *ISPRS J. Photogrammetry Remote Sens.*, vol. 92, pp. 79–97, 2014.
- [31] N. Homainejad and C. Rizos, "Application of multiple categories of unmanned aircraft systems (UAS) in different airspaces for bushfire monitoring and response," *Int. Arch. Photogramm. Remote Sens. Spatial Inf. Sci.*, vol. 40, 2015.
- [32] C. Toth and G. Józków, "Remote sensing platforms and sensors: A survey," *ISPRS J. Photogramm. Remote Sens.*, vol. 115, pp. 22–36, 2016.
- [33] M. Piras *et al.*, "Detailed geological mapping in mountain areas using an unmanned aerial vehicle: Application to the Rodoretto valley, MW Italian alps," *Geomatics Natural Hazards Risk*, vol. 8, no. 1, pp. 137–149, 2017.
- [34] X. Zheng, F. Wang, and Z. Li, "A multi-UAV cooperative route planning methodology for 3d fine-resolution building model reconstruction," *ISPRS J. Photogramm. Remote Sens.*, vol. 146, pp. 483–494, 2018.
- [35] Leica-Geosystems, "Leica DMC-III airborne digital camera," [EB/OL], Accessed: 2 May, 2020. [Online]. Available: https://leica-geosystems.com/-/media/files/leicageosystems/products/datasheets/leica_dmciii_ds.ashx?la=en&hash=07CD70CF2CB1F8CD7F02FA781549C980.
- [36] Somag, "Gyro stabilization mount-GSM 4000," [EB/OL], Accessed: Aug. 28, 2020. [Online]. Available: https://www.somag-ag.de/fileadmin/user_upload/GSM_4000/Dokumente/GSM4000_abstract_2019.pdf.



Haitao Zhao received the M.E. degree in cartography and geographic information system from Wuhan University, Wuhan, China, in 2006, and the Ph.D. degree in cartography and geographic information system from the Institute of Remote Sensing and Digital Earth, Chinese Academy of Sciences, Beijing, China, in 2013.

He is currently a Senior Engineer with the Aerospace Information Research Institute, Chinese Academy of Sciences. His research interests include flight management system, POS-supported aerial photogrammetry, hyperspectral remote sensing, and geometric rectification.



Bing Zhang (Fellow, IEEE) received the B.S. degree in geography from Peking University, Beijing, China, in 1991, and the M.S. and Ph.D. degrees in remote sensing from the Institute of Remote Sensing Applications, Chinese Academy of Sciences (CAS), Beijing, China, in 1994 and 2003, respectively.

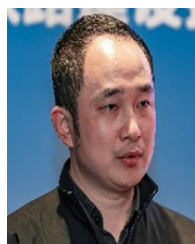
He is a Full Professor and the Deputy Director of the Aerospace Information Research Institute, CAS. He has developed five software systems in the image processing and applications. He has authored more than 300 publications, including more than 170 journal articles. He has edited six books/contributed book chapters on hyperspectral image processing and subsequent applications. His research interests include the development of mathematical and physical models and image processing software for the analysis of hyperspectral remote sensing data in many different areas.

Dr. Zhang has received 10 important prizes from Chinese government and special government allowances of the Chinese State Council. He has also received the National Science Foundation for Distinguished Young Scholars of China in 2013, and the 2016 Outstanding Science and Technology Achievement Prize of the Chinese Academy of Sciences, the highest level of awards for the CAS scholars. He is serving as an Associate Editor for the *IEEE Journal of Selected Topics in Applied Earth Observations and Remote Sensing*. He has been serving as a Technical Committee Member for IEEE Workshop on Hyperspectral Image and Signal Processing, since 2011, and as the President of Hyperspectral Remote Sensing Committee of China National Committee of International Society for Digital Earth, since 2012, and as the Standing Director of Chinese Society of Space Research (CSSR), since 2016. He is the Student Paper Competition Committee Member in International Geoscience and Remote Sensing Symposium (IGARSS) from 2015 to 2019.



Dong Li received the Ph.D. degree in signal and information processing from the University of Chinese Academy of Sciences, Beijing, China, 2016.

He is a Senior Engineer with the Aerospace Information Research Institute, Chinese Academy of Sciences. His research interests include LiDAR data processing and application.



Yalin Liu received the M.E. degree in remote sensing technology application from the China University of Geosciences, Wuhan, China, in 2007.

He is currently a Senior Engineer with China Railway First Survey and Design Institute Group Co., Ltd., Xi'an, China. His research interests include railway survey and design-related aerial surveys and application of new remote sensing technology.



Hong Yang received the master's degree in industry and business administration from Beihang University, Beijing, China, in 2010, and is currently working toward the Engineering Doctor degree with the School of Electronic Information, Northwestern Polytechnical University, Xi'an, China.

He is currently working with Aerospace Information Research Institute, Chinese Academy of Sciences, Beijing, China. His research interests include the overall design and application of high-resolution aerial remote sensing.



Wenmin Hu received the B.S. degree in information engineering and the master's degree in cartography and geoinformation system from Wuhan university, Wuhan, China, in 2004 and 2006 respectively, and the Ph.D. degree in cartography and geoinformation system from the Institute of Remote Sensing and Digital Earth, Chinese Academy of Sciences, Beijing, China, in 2013.

Since 2013, she has been with the University of Mining and Technology, Xuzhou, China. Her research interests include environmental remote sensing for mining areas, satellite image and laser-point cloud data processing and topographic mapping, and digital surface model (DSM) change and assessment.



Jie Pan received the B.S. degree in electronic engineering from the University of Electronic Science and Technology of China, Chengdu, China, in 2000, and the Ph.D. degree in communication and information system from the Chinese Academy of Sciences, Beijing, China, in 2019.

She is the Director of the Airborne Remote Sensing Center, Chinese Academy of Sciences. Her research interests include operation and engineering management of airborne remote sensing system.



Jianguo Liu received the bachelor's degree in electronics engineering from Tsinghua University, Beijing, China, in 1990, and the Ph.D. degree in cartography and remote sensing from the Chinese Academy of Sciences, Beijing, China, in 1999.

He is currently a Physical Scientist with the Science and Technology Branch, Agriculture and Agri-Food Canada, Canada.

His research interests include remote sensing for crop and soil biophysical parameters estimation, crop productivity, and agri-environmental sustainability

assessment.



Liuqing Xu received the B.S. degree in aircraft environment and life support engineering from the Beihang University, Beijing, China, in 2007, the M.S. degree in man-machine environmental engineering from the Beihang University, in 2012.

Since 2007, she has been with the Airborne Remote Sensing Center, Institute of Remote Sensing Applications, Chinese Academy of Sciences, Beijing, China. Her research interests include aircraft life cycle support and virtual maintenance.